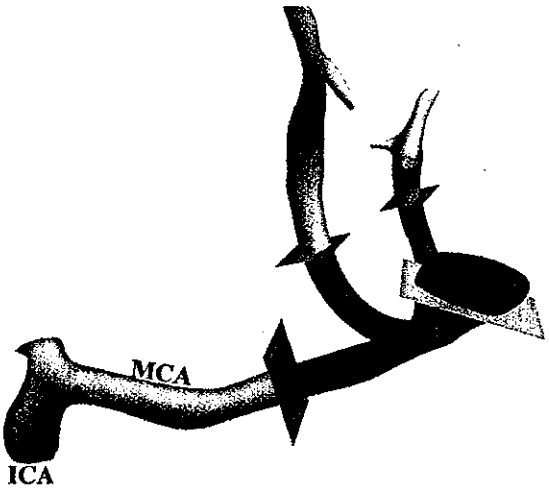

Figure 1. Extracted vessel image from 3-dimensional (3-D) computed tomographic angiography (after smoothing). The original model is trimmed out by the blue plane. The region to be analyzed (red) is divided into the aneurysm and the surrounding vessel by the yellow intersecting plane. ICA indicates internal carotid artery; MCA, middle cerebral artery.

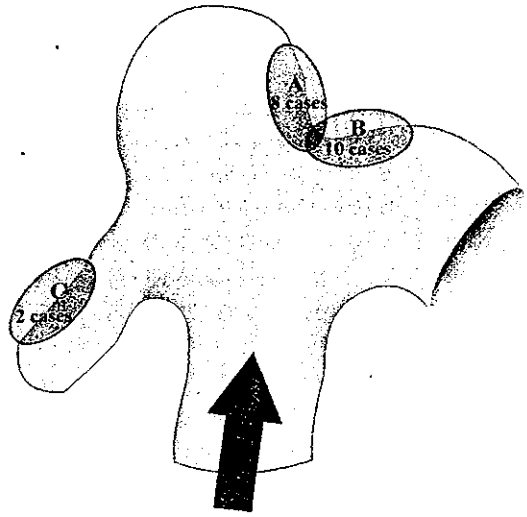

Figure 2. The sites where maximum wall shear stress (WSS) occurred in 20 cases. Eight occurred at the neck of the aneurysm (A), 10 at the origin of the branch artery in contiguity with the aneurysmal neck (B), and 2 in the branch vessel distant from the aneurysm (C).

statistical analysis of the magnitude of WSSs in and around saccular cerebral aneurysms.

Materials and Methods

Data Source

All medical data were acquired for diagnostic purposes, and consent for their use in this study was obtained from the patients or their closest relatives.

From January 2001 to December 2002, there were 42 middle cerebral artery (MCA) aneurysms that were diagnosed with 3-dimensional (3-D) computed tomographic (CT) angiography in 40 patients. Among them, 20 aneurysms of 19 patients had an adequate image quality for CFD calculation and were analyzed in this study. Patient population consisted of 7 men and 12 women, with a mean age of 61.5 years (range, 51 to 75 years). Three aneurysms were ruptured, and one of them was accompanied with an unruptured aneurysm. The other 16 aneurysms were detected before rupture by the screening examinations. All the aneurysm studied here were saccular aneurysms originating at the first major bifurcation of MCA.

Modeling of the Aneurysms

Three-dimensional CT angiography data with a voxel size of 0.21 mm×0.21 mm×0.50 mm were obtained with the aid of a multislice CT system,[16] the Aquilion multi 16 (Toshiba). The 16 central rows of 0.5-mm detector elements that were used had the following parameters: 0.75-second rotation, a scanning pitch of 0.69, 135 kV, and 260 mA. A total of 80 mL nonionic contrast medium (300 mg/mL) was injected at a rate of 3 mL/s via the median cubital vein. Digital images were transferred to a Unix workstation and vessel surfaces were constructed with the Fly-through mode of Alatoview (Toshiba). The fine irregularities of the original models resulting from partial volume effects or slice gaps were refined without changing the comprehensive geometry using our original smoothing software based on the algorithm of Garland mesh simplification[17] and Taubin mesh smoothing.[18] The aneurysm and the 20 mm of vessel surrounding it were trimmed out for the analysis. When possible, an intersecting plane dividing the aneurysm volume from that of the parent artery was made to allow a comparison of the WSS of the aneurysm and the vessel (Figure 1). Computational meshes were generated for these models with ≈60 000 hexahedral elements.

Numerical Simulation

CFD simulations were performed using our original finite-element solver under the governing equations of mass conservation and Navie–Stokes.[19–21] The boundary conditions were applied as follows. Blood was assumed to be an incompressible isothermal Newtonian fluid[22] with a specific gravity of 1000 kg/m^3 and a viscosity of 4.0×10^{-3} N/m^2 per second. The viscoelastic properties of the vessel wall were neglected and a rigid wall with no-slip condition was applied.[15] For the inlet condition, a pulsatile flow with a Womersley velocity profile was simulated,[23] with the typical MCA velocity obtained by transcranial Doppler scanning (mean velocity, 0.6 m/s; maximum velocity, 0.81 m/s; heart rate, 80 bpm). This inlet velocity condition was applied to all aneurysms (mean Reynolds number, 413; mean Womersley number, 3.99). A traction-free boundary condition[24] was applied to the outlets. The width of the time step for calculation was set at 0.0001 seconds.

To confirm numerical stability, the calculation was performed for 5 cardiac cycles and the result at the fifth cardiac cycle was used for

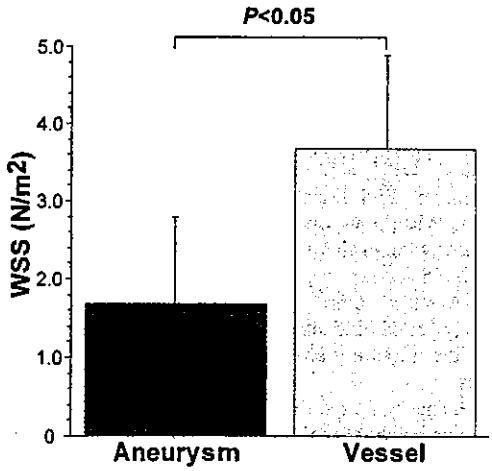

Figure 3. Comparison of WSSs between the aneurysm and vessel in 17 cases. The WSS of the aneurysm (red) is significantly lower than that of the vessel (yellow). Error bars indicate the standard deviation.

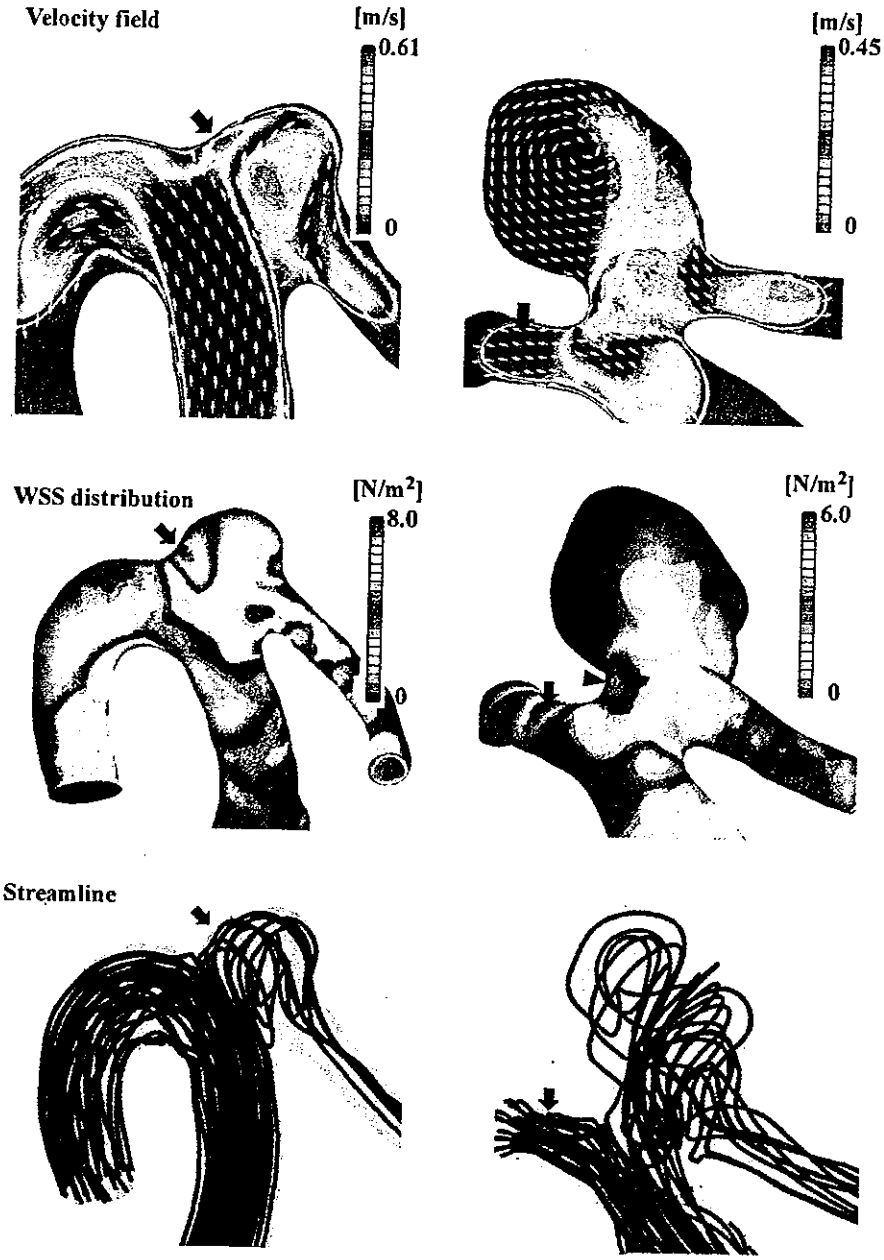

Figure 4. Visualization of the hemodynamics of 2 representative unruptured aneurysms (case 1, left; case 2, right). Arrows show the sites of maximum WSS. Top figures show velocity field in cross-sectional plane. Vectors show the direction of flow, and the magnitude of velocity is shown in colored contour. In case 1, interruption of flow at the bifurcation created a high-velocity field near the wall and caused a maximum WSS at the neck of the aneurysm. The intra-aneurysmal flow velocity was not decreased particularly in case 1. In contrast, in case 2, it was extremely low with a prominent recirculating zone in most parts of the aneurysm. Middle figures show WSS distribution in 3-D geometry. The maximum WSS occurred at the neck of the aneurysm in case 1. In case 2, a moderately high WSS occurred near the neck (arrow head), but the maximum WSS occurred at a site distant from the aneurysm where velocity increased as a result of reduction of the flow path. Bottom figures show the streamline, which shows the flow structure around the aneurysms. The lower part of the aneurysm in case 2 had flow structure similar to that in case 1. However, in case 2, the upper part had a stagnant disturbed flow structure, which led to a markedly low WSS.

the analysis. The calculation time for one aneurysm was ≈48 hours. WSS distributions were calculated from the 3-D velocity field data.[21]

Statistical Analysis

The maximum WSS region and its value were recorded for all aneurysms. When it was possible to divide the aneurysm from the parent artery with an intersecting plane, we calculated the spatially averaged WSS for each region at the peak systole. The WSS of the aneurysm was then compared with that of the vessel (paired Student *t* test). A nonpaired Student *t* test was applied to a comparison of the WSS of the ruptured aneurysms with that of the unruptured aneurysms.

For each aneurysm, the diameter of the inlet of the aneurysm and the maximum height of the aneurysmal sac from the inlet plane were measured from the 3-D model, and the aspect ratio was determined by dividing the latter by the former. Pearson correlation coefficients were calculated among the aspect ratio, the WSS of the aneurysm region, and the volumetric flow into the aneurysm. Statistical significance was taken as $P<0.05$.

Results

Magnitude and Distribution of WSSs

The sites where the maximum WSS occurred in the calculated region could be divided into 3 groups (Figure 2). In 10 aneurysms, the maximum WSS appeared at the origin of the branch artery in contiguity with the aneurysmal neck. In 8 aneurysms, the sites were at the neck of the aneurysm, and in the remaining 2 the maximum WSS occurred in the branch artery distant from the aneurysm. Whereas moderately high WSSs appeared at the body of the aneurysm in some cases, the WSSs at the tip or the bleb of the aneurysm were markedly low in all aneurysms. The peak WSS value averaged over the 20 cases was 14.39 ± 6.21 N/m^2 (mean$\pm$SD; 1 N/m^2=0.0075 mm Hg or 10 dyne/cm^2), which was 4-times higher than the spatially averaged WSS of the vessel region at the peak systole (3.64 ± 1.25 N/m^2).

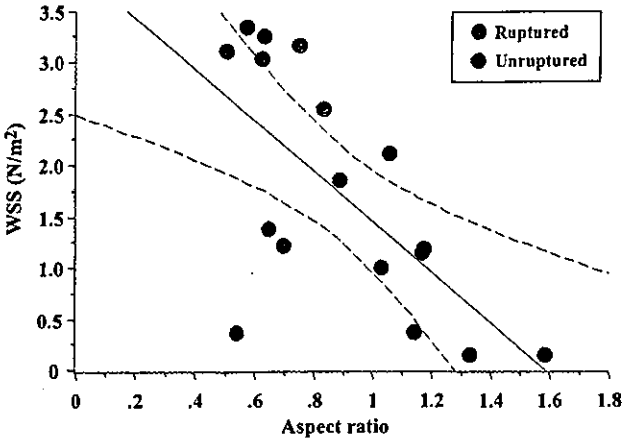

Figure 5. Bivariate scattergram with regression between the aspect ratio and the WSS of the aneurysm. A significant negative correlation can be observed ($r=-0.67$). Ruptured cases are shown as red, and unruptured cases are shown as blue. Dotted lines indicate 95% confidence bands.

Intersecting planes dividing the aneurysm from the parent artery were created successfully for all but 3 small unruptured aneurysms. For these 17 cases, the WSS of the vessel region (spatially averaged at the peak systole) was 3.64 ± 1.25 N/m^2. In contrast, the WSS of the aneurysm region (spatially averaged at the peak systole) was 1.64 ± 1.16 N/m^2, which is significantly lower than that of the vessel ($P<0.05$; Figure 3).

Flow Structure in the Aneurysms

The shape of the aneurysm had a profound impact on the flow structure within it. In case 1 (Figure 4, left), a small aneurysm with a smooth contour and a low aspect ratio of 0.56, the intra-aneurysmal flow velocity did not decrease particularly. The averaged WSS of the aneurysm region at the peak systole was 3.35 N/m^2, one of the highest among our cases. However, in case 2, which had a large aneurysm with an aspect ratio of 1.58 (Figure 4, right), the intra-aneurysmal flow velocity was markedly low and the flow field showed a conspicuous recirculating zone. In this case, the spatially averaged WSS of the aneurysm region was markedly low (0.14 N/m^2) even at the peak systole because of this large area of the flow stasis.

The aspect ratio of the aneurysm had a significant negative correlation ($r=-0.67$, $P<0.05$; Figure 5) with the WSS of the aneurysm region (spatially averaged at the peak systole). A mild positive correlation was observed between the spatially averaged WSS of the aneurysm region and the volumetric flow into the aneurysm ($r=0.50$, $P=0.06$). The correlation between the volumetric flow into the aneurysm and the aspect ratio of the aneurysm was weak ($r=0.36$, $P=0.06$).

Ruptured Versus Unruptured Aneurysms

The mean size (diameter) and the aspect ratio of the aneurysms were 3.36 mm and 0.73, respectively, for the ruptured cases (n=3) and 4.31 mm and 0.92, respectively, for the unruptured cases (n=17). The difference between the respective figure for the ruptured and unruptured cases was not statistically significant.

When the spatially averaged WSS of aneurysm region at the peak systole was compared between ruptured and unruptured cases, it was found to be significantly higher for ruptured cases (2.92 N/m^2 versus 1.48 N/m^2, $P<0.05$).

In all ruptured cases, high and low WSS were mixed in the small aneurysm area (Figure 6). The blood of parent artery flowed into the aneurysm more directly in the ruptured cases and high WSSs appeared at the body or the neck of aneurysm.

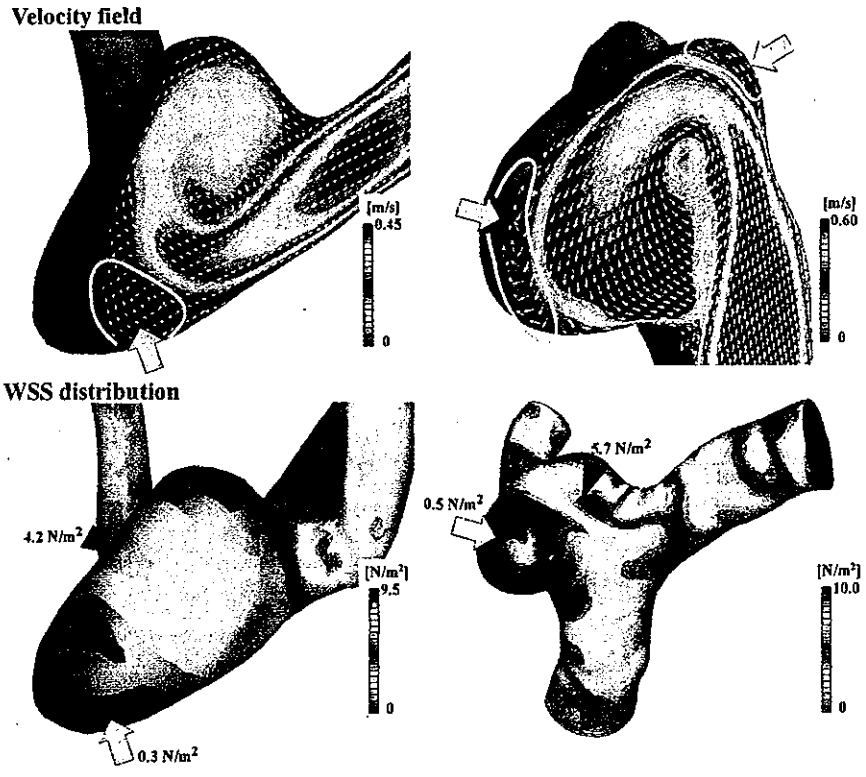

Figure 6. Velocity field and WSS distribution of 2 ruptured aneurysms. The velocity field in cross-sectional plane (upper) and the WSS distribution in 3-D geometry (lower) are shown in the same way as Figure 4. Black arrowheads indicate the site of moderately elevated WSSs in the aneurysm region. Yellow arrows and lines show the site of a markedly low WSS area and the flow stasis with recirculating zones at the tip of the aneurysm, respectively. The numbers near the arrows indicate the magnitude of WSSs at the sites.

This resulted in a higher averaged WSS of the aneurysm region in ruptured cases. However, at the tip, the stasis of the blood with recirculating zones was observed. This caused markedly low WSS at the tip (<0.5 N/m^2). These findings make fine contrast to the flow structure of the unruptured aneurysm, shown in the left side of Figure 4, which also had a high averaged WSS of the aneurysm region. The intra-aneurysmal velocity was not delayed, particularly near the wall. The WSS at the tip of this unruptured aneurysm was not decreased severely (1.7 N/m^2).

Discussion

This study demonstrates clearly that the magnitude of the WSS of the aneurysm region is significantly lower than that of the vessel region. The present study also disclosed that the WSS of the aneurysm region has a significant and inverse correlation with the aspect ratio of aneurysm, which has some connection to the rupture.[4,5]

WSS is a flow-induced stress that can be described as the frictional force of viscous blood.[10] The 3-D geometry and the 3-D velocity field of vessels are indispensable to the establishment of spatial distribution of WSS and the flow structure. In vivo measurements of the 3-D velocity field and WSS have become possible with the development of phase contrast magnetic resonance velocimetry for large and simple arteries like the aorta[25] or the carotid bifurcation.[13] However, in small and tortuous vessels like the intracranial arteries, the currently available techniques, like phase contrast magnetic resonance velocimetry, cannot be applied in calculating the spatial distribution of the WSS. To investigate the flow dynamics in cerebral arteries, simulation in vitro or by computer is necessary. The major difference between in vitro fluid experiments and CFD simulations may be the fact that the quality of computational mesh generation has some effect on the results of computer simulations. However, the reliability of computer simulations with proper mesh generation has been established.[24] Comparisons between our results and those of in vitro experiments are ongoing in our laboratory.[20]

Recent studies have indicated the involvement of WSS in the formation of saccular cerebral aneurysms.[11] A prolonged high WSS fragments the internal elastic lamina of vessels[26] and gives rise to the initial change involved in the formation of a cerebral aneurysm. Our results have established that the magnitude of the WSS of well-developed aneurysms is very low, in accordance with the previous hypothesis that the strength of the WSS of the aneurysm region is not sufficient to mechanically tear the wall of the aneurysm.[7] The WSS is converted to biological signals via mechanoreceptors on endothelial cells, and it modulates gene expressions and the cellular functions of the vessel wall.[9,10] It is assumed that a WSS of ≈2.0 N/m^2 is suitable for maintaining the structure of arterial vessels and a WSS lower than 1.5 N/m^2 will degenerate endothelial cells via the apoptotic cell cycle.[10] The WSS of the aneurysm region was barely 1.64 N/m^2 even in the peak systole and seems to be too low to maintain the regular cellar functions of endothelial cells. This excessively low WSS may be one of the main factors underlying the degeneration, indicating the structural fragility of the aneurysmal wall. Although a high WSS plays an essential role in the initiation of cerebral aneurysms,[11] a low WSS might be a major factor for its growth.

Our 3 ruptured aneurysms had higher averaged WSS of aneurysm region than unruptured aneurysms and they had markedly low WSS in their tip or bleb with high WSS in the body or fundus of aneurysm. We speculate that this low WSS at the tip or the bleb might be responsible for the fragile change of the aneurysm and led to the rupture. Endothelial cells react differently to the high and low WSS.[10] The proximity of high and low WSS in a small aneurysm region might enhance the degenerative change of the aneurysm wall.

Until now, there has been no study to our knowledge that demonstrated the changes of the size and the shape of the aneurysm immediately before and after the rupture. These changes might have affected our results. The current and previous[4,5] results of ruptured aneurysms might not characterize the aneurysm with high risk of rupture, but may only document the feature of the aneurysm after rupture. The application of these results to the clinical materials will prove the validity.

Conclusions

The results of this study suggest that the CFD technique has the potential to be a useful clinical tool for the prediction of the initiation, growth, and rupture of cerebral aneurysms.

References

1. Nakagawa T, Hashi K. The incidence and treatment of asymptomatic, unruptured cerebral aneurysms. *J Neurosurg*. 1994;80:217–223.
2. Hop JW, Rinkel GJ, Algra A, van Gijn J. Case-fatality rates and functional outcome after subarachnoid hemorrhage: a systematic review. *Stroke*. 1997;28:660–664.
3. Takagi K, Tamura A, Nakagomi T, Nakayama H, Gotoh O, Kawai K, Taneda M, Yasui N, Hadeishi H, Sano K. How should a subarachnoid hemorrhage grading scale be determined? A combinatorial approach based solely on the Glasgow Coma Scale. *J Neurosurg*. 1999;90:680–687.
4. Ujiie H, Tachibana H, Hiramatsu O, Hazel AL, Matsumoto T, Ogasawara Y, Nakajima H, Hori T, Takakura K, Kajiya F. Effects of size and shape (aspect ratio) on the hemodynamics of saccular aneurysms: a possible index for surgical treatment of intracranial aneurysms. *Neurosurgery*. 1999;45:119–129; discussion 129–30.
5. Weir B, Amidei C, Kongable G, Findlay JM, Kassell NF, Kelly J, Dai L, Karrison TG. The aspect ratio (dome/neck) of ruptured and unruptured aneurysms. *J Neurosurg*. 2003;99:447–451.
6. International Study of Unruptured Intracranial Aneurysms Investigators. Unruptured intracranial aneurysms–risk of rupture and risks of surgical intervention. International Study of Unruptured Intracranial Aneurysms Investigators. *N Engl J Med*. 1998;339:1725–1733.
7. Steiger HJ. Pathophysiology of development and rupture of cerebral aneurysms. *Acta Neurochir Suppl (Wien)*. 1990;48:1–57.
8. Stehbens WE. Etiology of intracranial berry aneurysms. *J Neurosurg*. 1989;70:823–831.
9. Gibbons GH, Dzau VJ. The emerging concept of vascular remodeling. *N Engl J Med*. 1994;330:1431–1438.
10. Malek AM, Alper SL, Izumo S. Hemodynamic shear stress and its role in atherosclerosis. *JAMA*. 1999;282:2035–2042.
11. Kondo S, Hashimoto N, Kikuchi H, Hazama F, Nagata I, Kataoka H. Cerebral aneurysms arising at nonbranching sites. An experimental study. *Stroke*. 1997;28:398–403; discussion 403–404.
12. Milner JS, Moore JA, Rutt BK, Steinman DA. Hemodynamics of human carotid artery bifurcations: computational studies with models reconstructed from magnetic resonance imaging of normal subjects. *J Vasc Surg*. 1998;28:143–156.
13. Papathanasopoulou P, Zhao S, Kohler U, Robertson MB, Long Q, Hoskins P, Xu XY, Marshall I. MRI measurement of time-resolved wall shear stress vectors in a carotid bifurcation model, and com-

parison with CFD predictions. *J Magn Reson Imaging*. 2003;17:153–162.
14. Steinman DA, Milner JS, Norley CJ, Lownie SP, Holdsworth DW. Image-based computational simulation of flow dynamics in a giant intracranial aneurysm. *AJNR Am J Neuroradiol*. 2003;24:559–566.
15. Jou LD, Quick CM, Young WL, Lawton MT, Higashida R, Martin A, Saloner D. Computational approach to quantifying hemodynamic forces in giant cerebral aneurysms. *AJNR Am J Neuroradiol*. 2003;24:1804–1810.
16. Katada K, Fujii N, Banno T, Nakane M. Usefulness of isotropic volumetric data in neuroradiological diagnosis. In: Reiser MF, Takahashi M, Modic M, Becker CR, eds. *Multislice CT*, 2nd revised ed. Berlin, Heidelberg, New York: Springer-Verlag; 2004:45–52.
17. Garland M, Heckbert PS. Surface simplification using quadric error metrics. In: *SIGGRAPH 97*. Los Angeles, California: ACM Press/Addison-Wesley Publishing Co; 1997:209–216.
18. Taubin G. Curve and surface smoothing without shrinkage. *The Fifth International Conference on Computer Vision (ICCV 95)*. Cambridge, Massachusetts: IEEE Computer Society; 1995:852–857.
19. Ooshima M, Takagi K, Hayakawa M. [Image-based simulation of cerebral aneurysms]. *Igaku Butsuri*. 2003;23:209–214. In Japanese.
20. Oshima M, Kobayashi T, Takagi K. Biosimulation and visualization: effect of cerebrovascular geometry on hemodynamics. *Ann N Y Acad Sci*. 2002;972:337–344.
21. Oshima M, Torii R, Kobayashi N, Taniguchi N, Takagi K. Finite element simulation of blood flow in the cerebral artery. *Comput Methods Appl Mech Eng*. 2001;191:661–671.
22. Brooks DE, Goodwin JW, Seaman GV. Interactions among erythrocytes under shear. *J Appl Physiol*. 1970;28:172–177.
23. Taylor CA, Hughes TJR, Zarins CK. Finite element modeling of blood flow in arteries. *Comput Methods Appl Mech Eng*. 1998;158:155–196.
24. Zienkiewicz OC, Taylor RL. *The Finite Element Method*, 4th ed. London, UK: McGraw-Hill; 1994.
25. Wood NB, Weston SJ, Kilner PJ, Gosman AD, Firmin DN. Combined MR imaging and CFD simulation of flow in the human descending aorta. *J Magn Reson Imaging*. 2001;13:699–713.
26. Masuda H, Zhuang YJ, Singh TM, Kawamura K, Murakami M, Zarins CK, Glagov S. Adaptive remodeling of internal elastic lamina and endothelial lining during flow-induced arterial enlargement. *Arterioscler Thromb Vasc Biol*. 1999;19:2298–2307.